Potentiometric titration study of $CaCO_3$ scaling control with non-water soluble polyetherimide and sulfonated polyetherimide films

Estefanía Correa-Muñoz[a,b,c], Nicole Butto-Miranda[b], Nicole Parra-Muñoz[a,d], Adriana Blanco-Leal[e], Alejandra Santa-Arango[f], Felipe Díaz-Soler[b], Mehrdad Yazdani-Pedram[g], Gustavo Cabrera-Barjas[h], Carlos Ostos-Ortiz[f], Franscisco Gracia[e], Andrónico Neira-Carrillo[b,*]

[a] Facultad de Ciencias Físicas y Matemáticas, Universidad de Chile, Avenida Beauchef 851, Santiago, 8370456, Chile.

[b] Departamento de Ciencias Biológicas Animales, Facultad de Ciencias Veterinarias y Pecuarias, Universidad de Chile, Santa Rosa 11735, La Pintana, 8820808, Chile.

[c] Aplicaciones en Termofluidos, Energía y Nanomateriales Avanzados – ATENA, Departamento de Ingeniería Mecánica, Universidad Francisco de Paula Santander Ocaña, Vía Acolsure, Ocaña, 546552, Colombia.

[d] Centro de Materiales para la Transición y Sostenibilidad Energética, Comisión Chilena de Energía Nuclear, Santiago, 7600713, Chile.

[e] Department of Chemical Engineering, Biotechnology and Materials, University of Chile, Beauchef 851, 6th Floor, Santiago, Chile.

[f] CATALAD Research Group, Instituto de Química, Facultad de Ciencias Exactas y Naturales, Universidad de Antioquia, Calle 70 No. 52-21, A.A. 1226, Medellín, Colombia.

[g] Departamento de Química Orgánica y Fisicoquímica, Facultad de Ciencias Químicas y Farmacéuticas. Universidad de Chile, Olivos 1007, Independencia, Santiago, 8380492, Chile.

[h] Facultad de Ciencias para el Cuidado de la Salud, Universidad San Sebastián, Campus Las Tres Pascualas, Lientur 1457, Concepción 4060000, Chile.

Corresponding author: Andrónico Neira-Carrillo, E-mail: aneira@uchile.cl

Preprint not peer reviewed

This preprint research paper has not been peer reviewed. Electronic copy available at: https://ssrn.com/abstract=4820270

Abstract

Automatic potentiometric titration (APT) is a tool used to study chemical reactions and the crystallization of $CaCO_3$ using additives. We demonstrates how APT is also valuable for studying the $CaCO_3$ crystallization using water-insoluble polymeric films, ideal for studies on scale formation on surfaces exposed to Ca^{2+} and CO_3^{2-} ions, ion exchange surfaces, or desalination membranes, etc. Polyetherimide (PEI) and sulfonated polyetherimide (SPEI) films were prepared by solvent casting technique, and their surface studied using FESEM, XPS, Z potential, and contact angle. APT assays were performed with polymer films, using a carbonate buffer (pH 9), dosed with $CaCl_2$, and monitoring free Ca^{2+}. The APT curves with PEI showed no significant difference compared to the control, while the presence of SPEI film affected the kinetics of $CaCO_3$ formation. This was evidenced by changes in the slope and peak maximum of the APT curves. FTIR, XRD, and FESEM of the polymeric films and the $CaCO_3$ after the APT assays showed control over the types of $CaCO_3$ polymorphs. We show that the SPEI film is a good candidate to delay the surface formation of $CaCO_3$ in water, through the adsorption of Ca^{2+} ions and the formation of pre-nucleation clusters of $CaCO_3$.

Keywords: Automatic potentiometric titration (APT), $CaCO_3$ scaling, polymer films, surface characterization, sulfonated polyetherimide (SPEI).

Preprint not peer reviewed

This preprint research paper has not been peer reviewed. Electronic copy available at: https://ssrn.com/abstract=4820270

1. Introduction

In general, the method of potentiometric titration belongs to the chemical methods of analysis in which the endpoint of titration is controlled by measuring the potential (voltage) in a solution through an indicator electrode based on the amount of the titrant added of exactly known concentration. This method of automatic potentiometric titration (APT) is particularly versatile since there are different indicator electrodes for titrating various chemical reactions. APT not only provides information about the endpoint of the titration but also describes the processes involved in the reaction through a curve and its different stages in real time. The experimental APT method consists of a pH or millivolt meter with high impedance, a beaker with a magnetic stirrer, indicator and reference electrodes, and a titrant dispenser [1].

APT is widely used in studies of calcium carbonate ($CaCO_3$) nucleation with different additives in solution. The titration of calcium ions (Ca^{2+}) allows for the study of interactions and influences of additives in the crystallization process. The recording of potential (i.e., curve) during APT allows for the quantification of bound ions, cluster formation and stabilization, nucleation inhibition, and the study of the control of the types of polymorphs that form [2] [3]. Understanding the nucleation and crystallization mechanisms of $CaCO_3$ is of great importance since it is the primary source of water hardness. Additionally, this salt is a biomineral present in various terrestrial and marine organisms. Industrially, it is very relevant because it is involved in many chemical processes, but it can also cause problems such as scale deposits in pipes, leading to metal corrosion and obstructing the proper functioning of equipment.

Crystallization assays using APT involve dosing $CaCl_2$ into a carbonate buffer solution, in the absence or presence of additives. Meanwhile, the ion-selective electrode for calcium allows the determination and understanding of the kinetics of free Ca^{2+} concentration from

Preprint not peer reviewed

This preprint research paper has not been peer reviewed. Electronic copy available at: https://ssrn.com/abstract=4820270

the measured potential data. In Fig. 1, a typical curve obtained in APT assays is shown. In the first stage (1), the concentration of free Ca^{2+} increases linearly with the addition of $CaCl_2$ to the buffer solution at a constant rate. In this pre-nucleation stage, the concentration of free Ca^{2+} is lower than the amount added when dosing the $CaCl_2$ due to the binding of Ca^{2+} ions to CO_3^{2-} ions in stable nucleation groups [4]. The slope of the curve in this stage provides relevant information about the formation of pre-nucleation clusters (PNC). The second stage (2), which corresponds to the peak of the curve, is the time at which nucleation occurs, and finally in stage (3), the amount of free Ca^{2+} falls to a lower level that represents the solubility of the precipitated $CaCO_3$ phase [4].

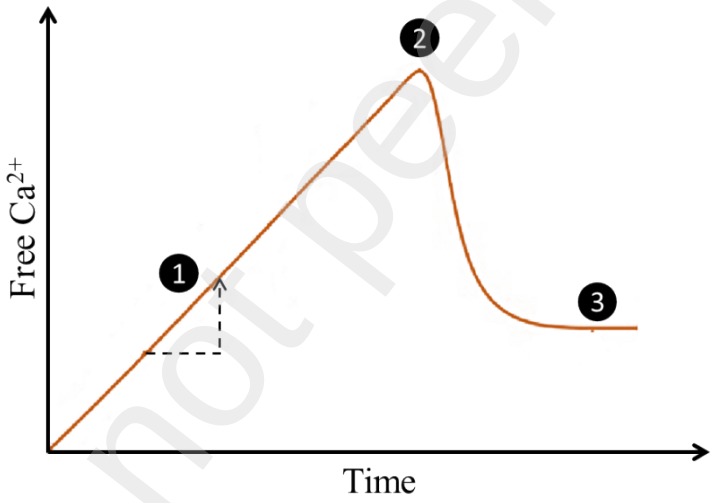

Fig. 1. APT curve of free Ca^{2+} in $CaCO_3$ crystallization assays. (1) Pre-nucleation slope; (2) Nucleation time; (3) Solubility of the precipitated $CaCO_3$ phase. Adapted from [3].

The effect of different additives in solution on the nucleation and crystallization of $CaCO_3$ through APT has been studied. Picker and colleagues [4] conducted APT assays using 20 naturally occurring amino acids. The results showed that several amino acids influence the crystallization of $CaCO_3$, with aspartic acid showing the most pronounced effects on the

Preprint not peer reviewed

This preprint research paper has not been peer reviewed. Electronic copy available at: https://ssrn.com/abstract=4820270

process. Such studies contribute to understanding the biomineralization processes that occur in nature influenced by biomolecules. On the other hand, Verch and colleagues propose the APT method as a valuable tool for studying the effect of antiscalants used in industry on the crystallization of $CaCO_3$. Therefore, sodium tripolyphosphate, citrate, polyacrylate, and polyaspartic acid were evaluated [5]. The authors demonstrate that these additives have an inhibitory effect since it takes longer for the nucleation of $CaCO_3$ to occur. Other similar studies have been conducted with polystyrene sulfonate and poly(styrene-alt-maleic acid) [5], peptides [6], and alginate [7].

It is noteworthy that in the mentioned research, all additives and polymers studied are solubilized in water. Here, we propose the APT method as a valuable tool for studying the effect of water-insoluble polymeric surfaces. Any interaction of Ca^{2+} ions with the polymeric surface is reflected in the APT curve, thus indirectly analyzing what occurs on the surface of interest. Understanding the effect of polymeric surfaces on the crystallization of $CaCO_3$ by APT would aid in comprehending the phenomena occurring in the formation of scale on surfaces of equipment, coatings, and membranes for reverse osmosis, water softening, distillation, and desalination [8–11].

In this work, the effects of polyetherimide (PEI) and sulfonated polyetherimide (SPEI) on the crystallization of $CaCO_3$ *in vitro* by APT is studied. For this, PEI and SPEI films were prepared by the solvent casting technique and characterized by various physicochemical techniques i.e., Fourier transform infrared spectroscopy (FTIR), field emission scanning electron microscopy (FESEM); X-ray diffraction (XRD), X-ray photoelectron spectrometer (XPS), elemental analysis, thermogravimetric analysis (TGA), and Z potential, before and after the $CaCO_3$ crystallization assays. The experimental results showed that the APT method is a valuable tool for understanding the effect of polymeric surfaces on the kinetics of

Preprint not peer reviewed

This preprint research paper has not been peer reviewed. Electronic copy available at: https://ssrn.com/abstract=4820270

nucleation, growth, and polymorphisms of $CaCO_3$. This information would be useful for potential industrial applications such as ion exchange surfaces or desalination membranes and crystallization, among others.

2. Experimental and methods

2.1. Materials and reagents

Polyetherimide ULTEM 1000 from SABIC Innovative Plastics and sulfonated polyetherimide obtained from the sulfonation reaction of PEI were used. For the sulfonation reaction, film preparation, and APT assays, the following reagents and solvents were used: chlorosulfonic acid for synthesis from Sigma-Aldrich; 1,2-dichloroethane EMPLURA® grade from Supelco, Merck; N,N-dimethylacetamide (DMAc) ReagentPlus® grade, 99%, monohydrated sodium carbonate (Na_2CO_3) ≥ 99.5% from Sigma-Aldrich; sodium bicarbonate ($NaHCO_3$) from TCL; calcium chloride ($CaCl_2$) for analysis; Reag. PhEur from Merck; sodium hydroxide (NaOH) EMSURE® ISO from Merck; and sodium chloride.

2.2. Synthesis of SPEI

SPEI was obtained by the sulfonation reaction of PEI using chlorosulfonic acid as the sulfonating agent following the methodology of Rajagopalan and colleagues [12] (Fig. 1S). Briefly, 10 g of PEI were dissolved in 50 mL of 1,2-dichloroethane at 60 °C under an inert atmosphere using argon. Once the solution cooled to room temperature, 2.06 mL of chlorosulfonic acid diluted in 35 mL of 1,2-dichloroethane was slowly added under vigorous stirring, taking about 1 h during the precipitation of SPEI. The resulting suspension was stirred for an additional 30 min. The obtained SPEI was precipitated in 50 mL of DMAc at 50 °C for 2 h. The SPEI solution at room temperature was precipitated drop by drop into 500

Preprint not peer reviewed

This preprint research paper has not been peer reviewed. Electronic copy available at: https://ssrn.com/abstract=4820270

mL of isopropyl alcohol. The SPEI pellets obtained were vacuum-filtered and washed 5 times with isopropyl alcohol. Finally, the product was dried in an oven at 50 °C for 48 h.

2.3. Preparation PEI and SPEI films

The PEI and SPEI films were prepared by solvent casting. Each polymer (300 mg) was dissolved in 5 mL of DMAc in a water bath at 60 °C for 2 h. Subsequently, the yellow solutions were poured into 10 cm diameter glass Petri dishes and covered with perforated aluminum foil. The Petri dishes were then placed in an oven at 80 °C for 48 h to evaporate the solvent. The PEI and SPEI films were allowed to cool slowly, removed, and stored until use.

2.4. Automatic potentiometric titration (APT) assays

For the $CaCO_3$ crystallization assays using APT, a Metrohm 907 Titrando titration system was used with a crystallization cell, two dosers ($CaCl_2$ and NaOH), three electrodes (pH, Ca^{2+} and conductivity), and film-sample holders. The APT assays involve slowly and automatically dosing 10 mM $CaCl_2$ at a flow rate of 10 µl/min into 35 mL of 10 mM carbonate buffer (pH 9) to form $CaCO_3$. The pH is kept constant at 9 by automatically adding 0.1 M NaOH. The free cation in the solution is monitored in real time with the selective Ca^{2+} electrode. The assays were conducted for 19,000 s (5.25 h) at 20 °C in duplicate in the absence and presence of PEI and SPEI films.

For the $CaCO_3$ crystallization assays in the presence of the films, a Teflon piece (Fig. 2S) designed to hold a sample circle of 15 mm in diameter was used, which was submerged in the buffer solution. The piece consists of a rod and cap; the sample is placed on the rod, and then the cap is used to hold the sample in place and prevent it from moving in the solution to ensure accurate electrode measurements. Additionally, with the use of the piece, no adhesive

Preprint not peer reviewed

This preprint research paper has not been peer reviewed. Electronic copy available at: https://ssrn.com/abstract=4820270

is needed that could interfere with the crystallization assays. The piece exposes an area of 154 mm^2 (circle of 14 mm diameter).

After completing the crystallization assay, the obtained $CaCO_3$ precipitate and the films were added to cold ethanol to stop the reaction. The $CaCO_3$ was stirred in cold ethanol for 30 min and then filtered. The $CaCO_3$ and PEI and SPEI films were washed several times with ethanol and dried in an oven for 24 h at 35 °C. From the data obtained from the assays, titration curves were constructed, and the slopes of the curves were determined from 2,000 s of reaction to the peak maximum and the nucleation times.

Prior to each APT assay, calibration measurements of the selective Ca^{2+} electrode were conducted using a NaCl solution with the same ionic strength as the carbonate buffer solution. The calibration assays were performed for 3,400 s, controlling the pH at 9 with 0.01M NaOH, and the concentration of free calcium over time was determined.

Before each assay, the crystallization cell, electrodes, Teflon piece, and films were washed with acetic acid solution at pH 3 and copious ultrapure water 18.25 MΩ.cm.

2.5. Characterizations

The synthesized PEI and SPEI were characterized on a Fisons EA1108 elemental analyzer using method LRR-P-EA-01 to determine the content of carbon, hydrogen, nitrogen, and sulfur (CHNS) with detection limits of C: 0.1% w/w; H: 0.7% w/w; N: 2% w/w; S: 2% w/w in dry and powdered samples. Fourier transform infrared spectroscopy spectra were obtained from a Thermo Scientific Nicolet iS10 spectrometer with Attenuated Total Reflectance in the range of 4000 cm^{-1} to 400 cm^{-1}. Thermogravimetric analysis was conducted on a NETZSCH TG 209 F3 Tarsus® instrument with a constant nitrogen flow of 30 mL/min and a temperature increase of 10 °C/min from room temperature up to 600 °C.

Preprint not peer reviewed

This preprint research paper has not been peer reviewed. Electronic copy available at: https://ssrn.com/abstract=4820270

188 The morphology of the PEI and SPEI films was observed on a Field Emission Gun Scanning
189 Electron Microscope FEI QUANTA FEG 250. The samples were previously metallized with
190 gold to a thickness of 5 nm. A Specs brand XPS (NAP-XPS) with a PHOIBOS 150 1D-DLD
191 analyzer was used to obtain information about the surface composition of the films. A
192 monochromatic Al-Kα source (1486.7 eV, 13 kV) with a pass energy of 85.36 eV for general
193 spectra and 20 eV for high-resolution spectra was used. The step size was 1 eV for general
194 spectra and 0.1 eV for high-resolution spectra. Twenty measurement cycles were performed
195 for high-resolution spectra and five for general spectra. A charge compensation of 3 eV and
196 20 μA was used. The Z potential of the film surfaces was measured on a SurPASS™ 3
197 electrokinetic analyzer for solid-surface analysis from Anton Paar. Used was 200 mL of a
198 0.001M KCl solution (ultrapure water), and an automatic pH sweep from 1-10 was performed
199 using 0.05 M NaOH and 0.05M HCl solutions for control. To study the wettability of the
200 films, a contact angle meter OCA 15EC from Dataphysics using ultrapure water 18.25
201 MΩ.cm was used. Samples were adhered with double-sided tape to glass slides. Five contact-
202 angle measurements were taken per sample.
203 After the APT crystallization assays, the obtained $CaCO_3$ and the PEI and SPEI films were
204 characterized by FTIR, XRD, transmission electron microscopy, and FESEM. Obtained were
205 the XRD patterns of the $CaCO_3$ powder on a BRUKER D2 PHASER diffractometer equipped
206 with a LYNXEYE detector using Cu Kα radiation (λ = 0.15406 nm) with a sweep from 3 to
207 80° 2θ, with a step of 0.01°. To determine the proportion of vaterite and calcite in the $CaCO_3$
208 precipitate, the equation proposed by Kontoyannis was used [13] based on the XRD pattern.

209 $$\frac{I_c^{104}}{I_v^{110}} = \Delta \times \frac{X_c}{X_v},\ \Delta = 7.691 \quad (1)$$

Preprint not peer reviewed

This preprint research paper has not been peer reviewed. Electronic copy available at: https://ssrn.com/abstract=4820270

$$X_v = \frac{7.691 I_v^{110}}{I_c^{104} + 7.691 I_v^{110}};\ X_c = 1 - X_v \quad (2)$$

where, Δ is a proportionality constant, I_c^{104} and I_v^{110} are the intensities of the (104) planes of calcite and (110) of vaterite, respectively, and X_c and X_v correspond to the molar percentages of the calcite and vaterite phases, respectively. The XRD patterns of the films were obtained on a Siemens D-5000 diffractometer using CuKα radiation with a sweep from 3 to 80° 2θ, with a step of 0.02. Finally, amorphous calcium carbonate (ACC) from the precipitate was observed using a Philips Tecnai 12 (Biotwin) transmission electron microscopy operating at 120 kV.

3. Results and discussion

3.1. Synthesis of SPEI

Elemental analysis provided quantitative information on the mass percentage of CHNS in the PEI and SPEI samples (Table 1). The presence of sulfur was confirmed for SPEI and is absent in PEI, demonstrating the incorporation of the sulfonic group (SO_3H) into the PEI polymer.

Preprint not peer reviewed

This preprint research paper has not been peer reviewed. Electronic copy available at: https://ssrn.com/abstract=4820270

Table 1. Elemental analysis of the PEI and SPEI samples

Samples	Analysis	Results ± RSD
PEI	Carbon (C)	73.94 %- w/w ± 0.64
	Hydrogen (H)	4.26 %- w/w ± 2.7
	Nitrogen (N)	4.62 %- w/w ± 0.94
	Sulfur (S)	< %- w/w [1]
SPEI	Carbon (C)	63.63 %- w/w ± 2.0
	Hydrogen (H)	4.10 %- w/w ± 2.0
	Nitrogen (N)	4.9 %- w/w ± 2.0
	Sulfur (S)	4.58 %- w/w ± 2.0

[1] result not detectable, detection limit reported.

Furthermore, the mass percentage of sulfur (%S) was used to determine the degree of sulfonation of the polymers, which is defined as the molar ratio between sulfonic groups and the repeating unit of the polymer. The relationship between %S and the degree of sulfonation was established and plotted (Fig. 3S). The obtained second-degree equation was:

$$DS = 0.0056\ (\%S)^2 + 0.1832(\%S) + 0.0006 \quad (3)$$

where %S corresponds to the mass percentage of sulfur. The degree of sulfonation of SPEI was 0.95 (95%).

Fig. 2a and 2b present the FTIR and TGA results of the PEI and SPEI polymers, respectively. Fig. 2a shows the FTIR spectra of both polymers featuring characteristic absorption bands of polyetherimide, asymmetric and symmetric stretching of the carbonyl C=O of the imides at

Preprint not peer reviewed

This preprint research paper has not been peer reviewed. Electronic copy available at: https://ssrn.com/abstract=4820270

1718 cm-1, C=C stretching of aromatic rings at 1598 cm^{-1}, C-N group stretching at 1476 cm^{-1} and 744 cm^{-1}, symmetric bending of the methyl groups in the isopropylidene unit at 1352 cm^{-1}, and aromatic ether C-O-C at 1233 cm^{-1}. In the spectrum of SPEI, the presence of -SO_3H was confirmed with the appearance of new bands at 3475 cm^{-1}, 1160 cm^{-1}, 1090 cm^{-1}, and 1020 cm^{-1}, similar to what is reported in the literature [12] [14] [15].

On the other hand, the thermal stability of PEI and SPEI was studied by TGA-differential thermogravimetry (Fig. 2b). Exhibited by PEI was a single mass loss stage (32.0 2%), with its maximum rate of thermal decomposition at 540.1 °C. In contrast, SPEI showed three stages of mass loss. The first stage, occurring after 100 °C, is attributed to traces of residual solvents from the synthesis process. A second stage, with a maximum rate of decomposition at 319.4 °C and associated with a mass loss of 8.4%, occurs due to the loss of SO_3H groups, confirming the successful sulfonation of SPEI [12]. Finally, the third stage shows a maximum decomposition temperature at 530.0°C (mass loss 29.4%) and corresponds to the decomposition of the rest of the polymeric chain, which coincides with the thermal decomposition of unmodified PEI. These results indicate that the sulfonated polymer is less thermally stable than the original polymer.

Preprint not peer reviewed

This preprint research paper has not been peer reviewed. Electronic copy available at: https://ssrn.com/abstract=4820270

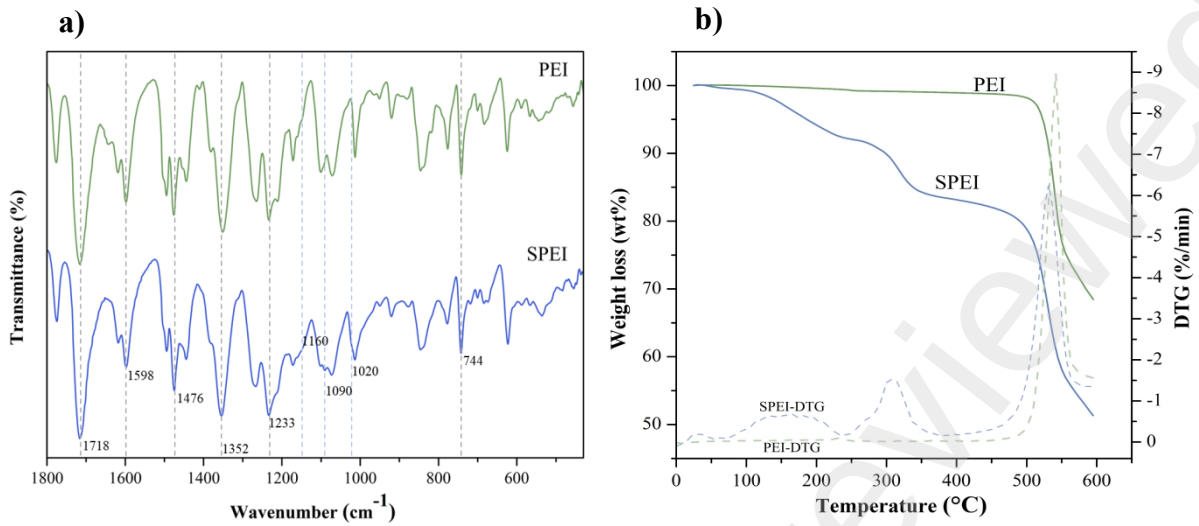

Fig. 2. a) FTIR spectra and b) TGA analysis of PEI and SPEI.

3.2. PEI and SPEI films

The solvent casting technique allowed for the preparation of PEI and SPEI films and analyzed by optical (Fig. 4S) and FESEM (Fig. 5S) techniques. Fig. 4S shows that the optical images of the PEI and SPEI films were translucent with a slight yellowish tint characteristic of the polymer. The thicknesses of the PEI and SPEI films were 46 ± 3 μm and 27 ± 1 μm, respectively. The reduction in thickness of the SPEI relative to the PEI is related to the volumetric contraction of the polymer due to the formation of hydrogen bonds between the sulfonic groups of the different polymeric chains. In Fig. 5S, FESEM micrographs of the surface of the PEI (Fig. 5Sa) and SPEI (Fig. 5Sb) films are presented, respectively. Both images show smooth, homogeneous surfaces free of cracks, as expected when using the solvent casting technique. The slow evaporation of the solvent allows for the uniform distribution of both polymers' chains in the used mold.

Preprint not peer reviewed

This preprint research paper has not been peer reviewed. Electronic copy available at: https://ssrn.com/abstract=4820270

Additionally, the surface composition of the films was investigated by XPS. Fig. 3a displays the general XPS spectra of the PEI and SPEI films; Fig. 3b and 3c present the XPS spectra of the C1s region of the PEI and SPEI films, respectively; Fig. 3d and 3e show the XPS spectra of the O1s region of the PEI and SPEI films; and Fig. 3f presents the XPS spectrum of the S2p region of the SPEI film. In Fig. 3a, the spectrum of the PEI film exhibits three main peaks from the C1s, O1s, and N1s signals at binding energies of 284.5 eV, 531.5 eV, and 400.5 eV, respectively. Meanwhile, the spectrum of the SPEI film shows, in addition to the peaks of the C1s, O1s, and N1s signals, S2s signals at 232.0 eV and S2p at 168.0 eV, demonstrating the presence of the sulfur atom of the sulfonic group.

Preprint not peer reviewed

This preprint research paper has not been peer reviewed. Electronic copy available at: https://ssrn.com/abstract=4820270

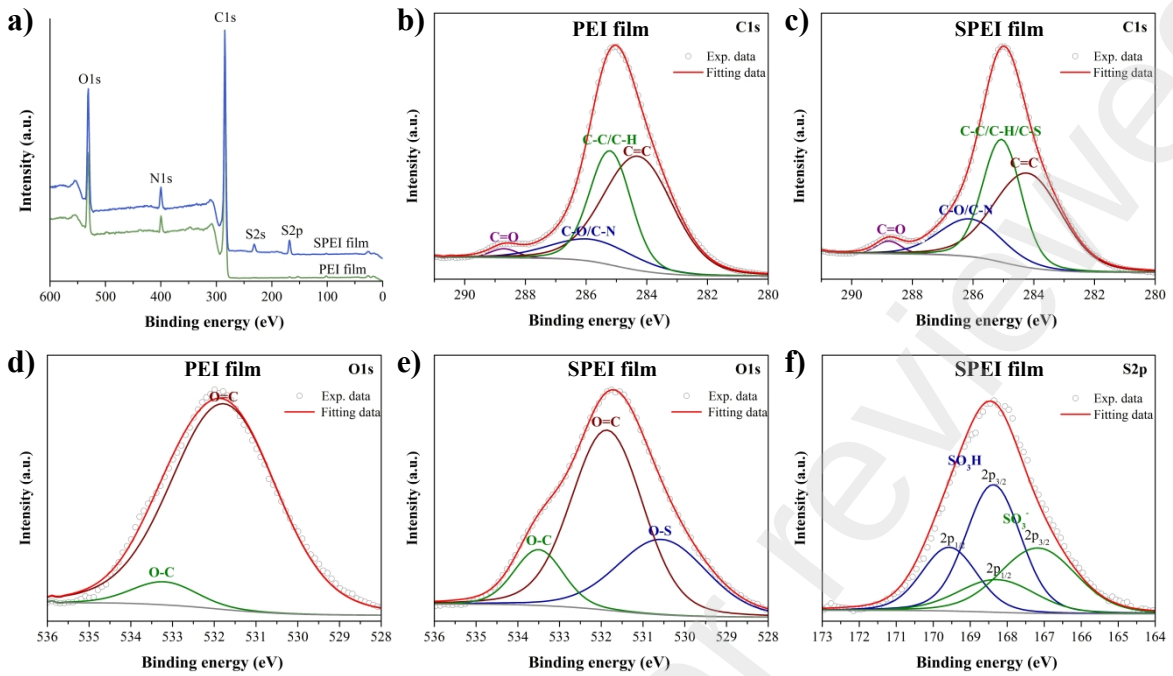

Fig. 3. a) XPS spectra of PEI and SPEI films, b) C1s region of PEI, c) C1s region of SPEI, d) O1s region of PEI, e) O1s region of SPEI, and f) S2p region of SPEI.

In Fig. 3b and 3c, the C1s spectra of both films were adjusted to four peaks. For PEI films, the peak at 284.3 eV was assigned to the carbons present in C=C bonds; the peak at 285.2 eV to C-C and C-H bonds; at 285.8 eV to C-O and C-N bonds; and at 288.7 eV to C=O, similar to what has been reported for films [16][17][18] and electrospun meshes [19] of PEI. For the SPEI film, the peak at 285.2 eV was assigned not only to C-C and C-H bonds but also to C-S, as it has been reported that carbon linked to the sulfonic group is found at binding energies of 285.2 eV [20]. In Fig. 3d, the O1s spectrum of the PEI film was adjusted to two peaks at 531.6 eV and 533.1 eV assigned to the oxygens of the C=O bonds of the imides and C-O of the esters respectively, as has been reported [16][17][19]. As for the O1s spectrum of SPEI film in Fig. 3e, an additional peak was adjusted compared to the PEI film, at 530.6 eV,

Preprint not peer reviewed

This preprint research paper has not been peer reviewed. Electronic copy available at: https://ssrn.com/abstract=4820270

299 confirming the presence of the oxygens of the -SO_3H group on the surface of the SPEI film
300 [20].
301 The spectrum of the S2p region of the SPEI film in Fig. 3f was adjusted to two doublets.
302 Each doublet presents an energy difference of approximately 1.18 eV and a relative intensity
303 between the spins $2p_{3/2}$:$2p_{1/2}$ of 2:1. The doublet at the lower binding energy with peaks at
304 168.4 eV for $2p_{1/2}$ and 167.3 eV for $2p_{3/2}$ was assigned to the sulfur atoms of the SO_3^- group
305 in its anionic form, and the doublet at higher binding energy at 169.7 eV for $2p_{1/2}$ and 168.5
306 eV for $2p_{3/2}$ was assigned to the sulfur atoms in its neutral form SO_3H. The assignment of
307 two doublets for the anionic and neutral forms of the sulfonic group has been reported [21].
308 Researchers suggest that the anionic form presents higher electron density than the neutral
309 form, thus affecting the chemical environment of the sulfur, which is reflected in a lower
310 binding energy. Regarding the deprotonation of the -SO_3H group, this may be associated with
311 the polar solvent DMAc used, which would act as a base capturing protons from the medium,
312 and after the evaporation of the solvent, the hydrogen bond is not reformed [22][23].
313 The atomic percentage composition (%-atoms) of the surface of the PEI and SPEI films was
314 compared with the results of the elemental CHNS analysis. As shown in Table 2, the atomic
315 percentage composition of the surface obtained by XPS notably differs from the bulk
316 composition of the material obtained by elemental analysis (CHNS). This difference occurs
317 due to the interactions of the polymer within the bulk and the preparation methodology
318 [24][25]. Therefore, during the film-preparation process, the polymer interacts with DMAc
319 molecules through both nitrogen atoms and their carbonyl groups [26], and by forming
320 hydrogen bonds with the sulfonic group, generating an interaction towards the interior of the
321 solution volume. This could explain a lower O/C ratio obtained by XPS compared to the

Preprint not peer reviewed

This preprint research paper has not been peer reviewed. Electronic copy available at: https://ssrn.com/abstract=4820270

elemental CHNS analysis. However, a higher O/C ratio in the SPEI film compared to the PEI is noticeable, indicating that the surface was enriched with oxygen.

Table 2. Atomic percentage composition (%-atoms) of the surface of the PEI and SPEI films by XPS and of their bulk by elemental CHNS analysis.

% - atoms	**C**		**O**		**O/C**		**N**		**S**	
	XPS	CHNS	XPS	CHNS	XPS	CHNS	XPS	CHNS	XPS	CHNS
PEI	85.67	82.95	11.14	14.46	0.13	0.17	3.20	2.59	0.00	0.00
SPEI	77.31	74.96	15.39	20.13	0.20	0.27	4.23	2.89	3.07	2.02

Fig. 4a and 4b display the Z potential and the contact angle of the PEI and SPEI films, respectively. Fig. 4a shows that the PEI film presented its isoelectric point at approximately pH 3, similar to what has been reported by other authors [27] and slightly lower than the isoelectric point of an inert polymer (pH 4). The Z potential of the PEI film decreases with increasing pH. The carbonyls of the imides can contribute to the negative charge of the surface, as the oxygens in the double bond have a partial negative charge. Additionally, the adsorption of hydroxyl ions (OH^-) also contributes to the negative Z potential of the sample, which is more pronounced at high pH where there is a higher concentration of OH^- [28]. The Z potential of the SPEI film mainly shows negative values for the evaluated pH due to the negative charge of the sulfonic group. However, the Z potential does not reach as negative values as those of the PEI film; this is because the sulfonic group attracts water molecules (neutral), causing the total electrokinetic charge density to decrease, which is favored in basic pH where more sulfonic groups lose protons, and their negative charge interacts with more

Preprint not peer reviewed

This preprint research paper has not been peer reviewed. Electronic copy available at: https://ssrn.com/abstract=4820270

water molecules [28]. The behavior of both curves demonstrates the successful conversion of hydrophobic PEI to hydrophilic SPEI [28]. It is important to note that at the end of the SPEI film curve, at pH above 9, the Z potential shows a slight increase, indicating water absorption and swelling of the material, affecting the Z potential measurement as the interface between the water and the material is modified [28]. Complementarily, in Fig. 4b, the contact angle of both films is presented, showing a decrease in the contact angle of the PEI film compared to the SPEI film. Given that the smooth morphology of the films was similar (see Fig. 5S), the decrease in contact angle is attributed to the inclusion of the sulfonic group, which improves the hydrophilicity of SPEI, as observed in the Z potential results.

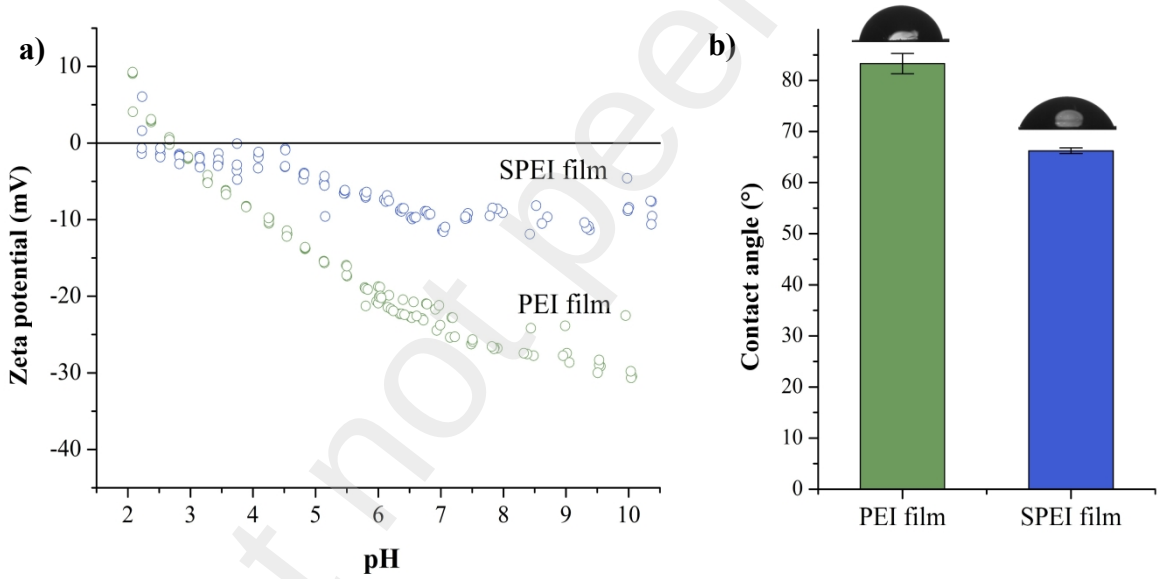

Fig. 4. a) Z potential at different pH levels and b) contact angle of PEI and SPEI films.

3.3. Potentiometric titration curves of crystallization assays

In Fig. 5a, the APT curves of the $CaCO_3$ crystallization assays in the absence of an additive (control) and in the presence of PEI and SPEI films are presented. The behavior of the APT curves is typical for $CaCO_3$ crystallization assays. All curves show an initial slope less than

Preprint not peer reviewed

This preprint research paper has not been peer reviewed. Electronic copy available at: https://ssrn.com/abstract=4820270

that of the added calcium, indicating a decrease in free calcium ions due to binding with carbonate ions forming $CaCO_3$ clusters. After reaching a maximum, at which point the nucleation stage occurs, the APT curve takes a negative slope as the free calcium is consumed in the growth of the particles. Finally, the curve reaches a constant free calcium concentration due to the equilibrium between dissolution and particle growth. Regarding the difference in the behavior of the APT curves, it is noted that the APT curves of the control assay and with the PEI film are similar, while the use of the SPEI film differs completely, indicating that the SPEI film significantly affects the crystallization process of $CaCO_3$. It is important to highlight two behaviors of the SPEI film curve: first, the nucleation time is longer (14815 ± 25 s) compared to the control (12405 ± 575 s) and the PEI film (12310 ± 460 s) (Fig. 5b), indicating that SPEI film acts as an inhibitor of $CaCO_3$ nucleation; secondly, the SPEI film curve showed an initial pre-nucleation slope of $9.2\times10^{-4} \pm 0.3\times10^{-4}$ μmoles/s (Fig. 5c), which was lower than the similar values obtained for the control assay ($11.0\times10^{-4} \pm 0.2\times10^{-4}$ μmoles/s) and PEI film ($10.5\times10^{-4} \pm 0.2\times10^{-4}$ μmoles/s), which is associated with the surface adsorption of Ca^{2+} ions to the film reducing their concentration in the medium affecting the formation and aggregation of PNC (Fig. 5c).

Subsequently, there is a change in slope at approximately 7,000 s, to a value of $7.6\times10^{-4} \pm 0.1\times10^{-4}$ μmoles/s. This indicates an increase in the amount of calcium that is adsorbed onto the film. We believe that the slope change is due to the greater capacity of the SPEI film to capture PNC that aggregate and grow on the surface, consuming calcium from the medium. A similar behavior has been observed in studies of $CaCO_3$ crystallization with polyacrylic acid in solution [3]. The inhibition effect promoted by the SPEI film may be associated with the adsorption of calcium on the film and the adsorption of PNC, requiring more time to reach maximum saturation.

Preprint not peer reviewed

This preprint research paper has not been peer reviewed. Electronic copy available at: https://ssrn.com/abstract=4820270

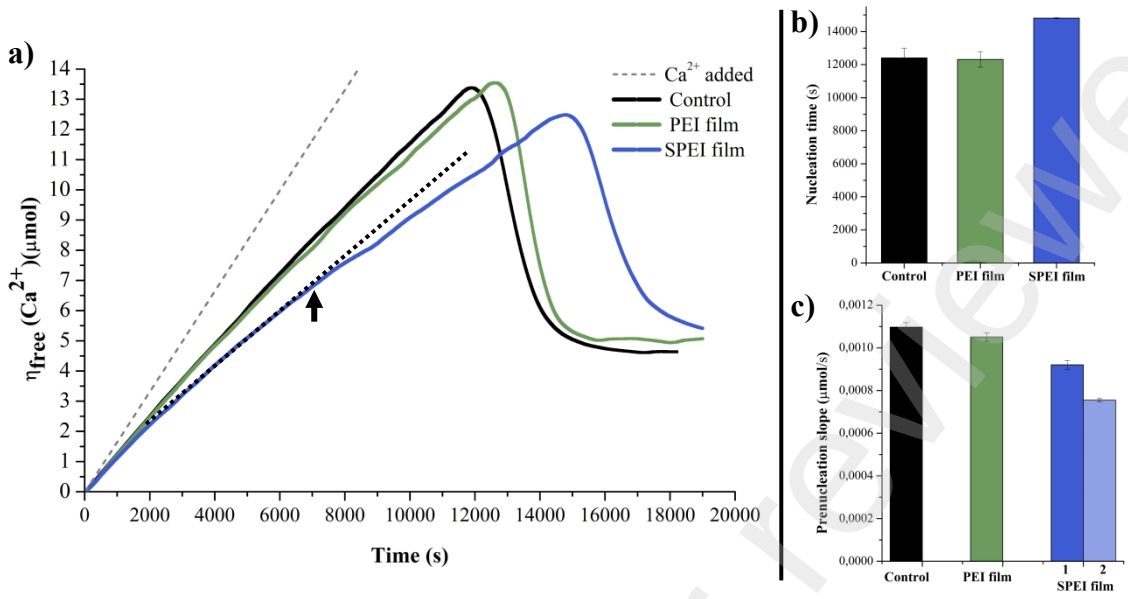

Fig. 5. a) APT curves of $CaCO_3$ crystallization assays in the absence and presence of PEI and SPEI films, b) nucleation time, and c) pre-nucleation slope of the APT curves.

To confirm the information from the APT curve, the precipitates and films after the crystallization of $CaCO_3$ were studied using FTIR, XRD, and FESEM.

3.4. Characterization of films and $CaCO_3$ precipitate after crystallization assays

In Fig. 6, the FTIR spectra of the $CaCO_3$ precipitates obtained in the absence (Fig. 6a) and presence of PEI (Fig. 6b) and SPEI (Fig. 6c) films are presented. The spectra show the typical absorption bands of the carbonate ion divided into four parts. Between 1390 – 1500 cm^{-1}, the absorption band of asymmetric stretching (ν_3), around 1080 cm^{-1} the band of symmetric stretching of the ion (ν_1, inset 1), at 875 cm^{-1} the out-of-plane bending of the ion (ν_2), and near 700 cm^{-1} the in-plane bending of the ion (ν_2, inset 2). In Fig. 6d, the inset 1 shows two absorption bands at 1089 cm^{-1} and 1074 cm^{-1} present both in the control and in the $CaCO_3$ precipitates obtained in the presence of PEI and SPEI films. It has been reported that the

Preprint not peer reviewed

This preprint research paper has not been peer reviewed. Electronic copy available at: https://ssrn.com/abstract=4820270

absorption band at 1089 cm^{-1} is accompanied by a band of lower intensity at 1076 cm^{-1} for the vaterite phase; however, it has also been reported that the band at 1074 cm^{-1} belongs to $CaCO_3$ in its amorphous form (ACC) [29]. Therefore, it is possible that both phases are present, particularly in the $CaCO_3$ precipitate in the presence of the SPEI film where the absorption band at 1074 cm^{-1}, which is more intense, suggests a higher concentration of ACC. On the other hand, in Fig. 6e, the vaterite phase, another polymorph can be identified in inset 2, the, the band at 712 cm^{-1} that corresponds to calcite. Particularly, the absorption band of calcite is more intense for the spectrum of $CaCO_3$ in the presence of PEI film than in the control and SPEI film. At 744 cm^{-1}, the absorption band of vaterite is found in all spectra.

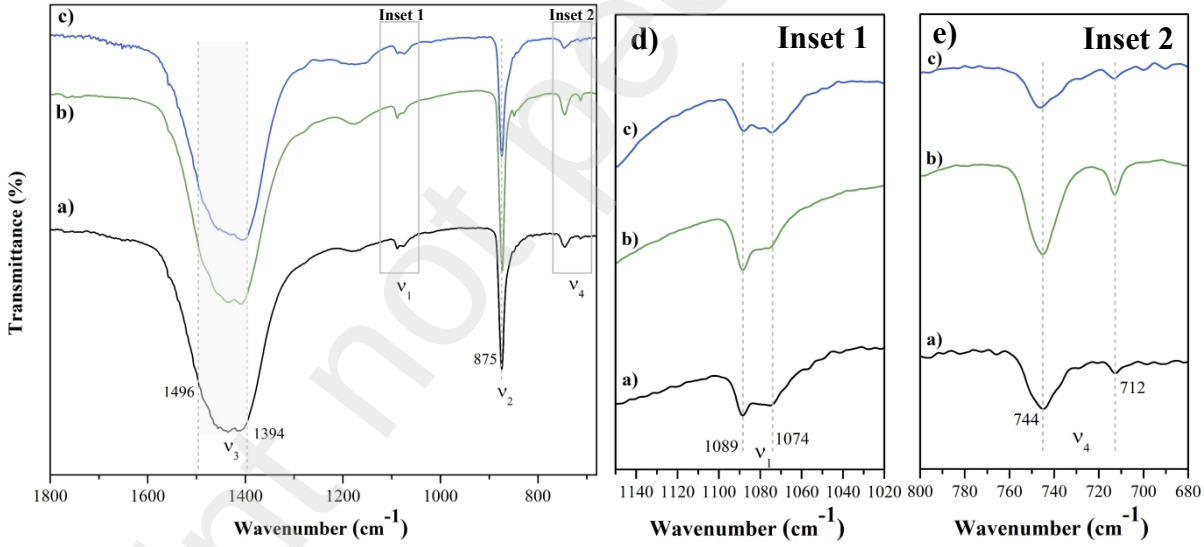

Fig. 6. FTIR spectra of $CaCO_3$ obtained from the $CaCO_3$ crystallization assays in the a) absence, in the presence of b) PEI or c) SPEI films, and d,e) spectra from insets 1 and 2.

In Fig. 6S and Fig. 7 (a-c), the spectra of PEI and SPEI films before and after the $CaCO_3$ crystallization assays are compared, respectively. In Fig. 6S, the absorption bands of PEI film

Preprint not peer reviewed

This preprint research paper has not been peer reviewed. Electronic copy available at: https://ssrn.com/abstract=4820270

414 did not undergo changes in intensity or shifts after the crystallization assays, while in SPEI
415 in Fig. 7 (a,b), very noticeable changes are observed. The inset of Fig. 7c shows the area of
416 the spectrum where the most significant changes occurred. The absorption band at 1021 cm^{-1}
417 underwent an increase in its intensity and shifted to a higher wavenumber at 1023 cm^{-1}, and
418 the absorption band at 1090 cm^{-1} experienced a slight shift and an increase in intensity located
419 at 1091 cm^{-1}. These absorption bands correspond to the sulfonate anion, which are sensitive
420 to interactions with the medium [15]. It is possible that the change occurred due to the
421 formation of a complex between the sulfonic group and the Ca^{2+} ions. The formation of this
422 coordination bond has been reported in studies with polystyrene sulfonate [30], in calcium
423 sulfonate complex greases [31], and indigo carmine complexes [32]. The formation of this
424 complex is related to the behavior of the APT curve, where the initial slope change of the
425 SPEI film compared to the PEI film and the control is due to the adsorption of the Ca^{2+} ions
426 onto the film. This demonstrates that the APT method for $CaCO_3$ crystallization studies in
427 the presence of polymeric surfaces provides valuable information for understanding aspects
428 of nucleation in real-time.

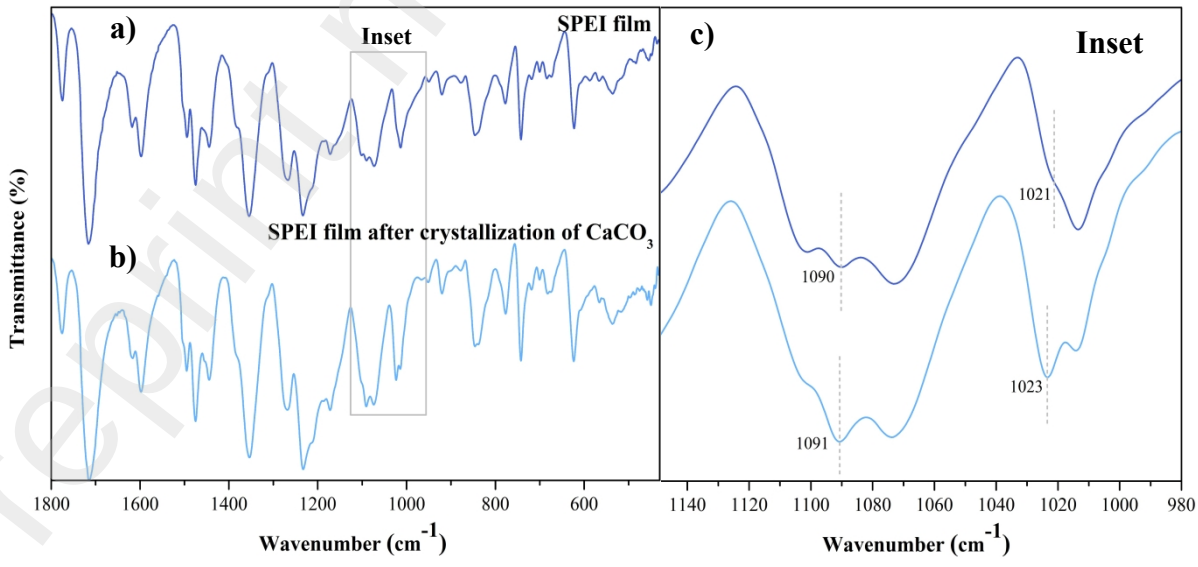

429

Preprint not peer reviewed

This preprint research paper has not been peer reviewed. Electronic copy available at: https://ssrn.com/abstract=4820270

Fig. 7. FTIR spectra of SPEI film a) before, b) after and c) insets spectra of SPEI film in the $CaCO_3$ crystallization assays.

In Fig. 8a, the XRD diffractograms of $CaCO_3$ in the absence (control) and presence of PEI and SPEI films are shown. The diffraction peaks were assigned using the ICDD database for $CaCO_3$ polymorphs (vaterite #033-0268 and calcite #005-0586). The crystallographic peaks for vaterite were found at 21.11° (004), 25.00° (110), 27.20° (112), 32.90° (114), 43.94° (300), 49.24° (304), 50.17° (118), and 55.90° (224) and for calcite at 23.14° (012), 29.48° (104), 36.05° (110), 39.49° (113), 43.22° (202), 47.55° (018), and 48.57° (116). In the control assay, both calcite and vaterite were identified in the same phases found in the presence of the PEI film. Particularly, the diffraction pattern of $CaCO_3$ with SPEI film showed primarily crystalline phases of vaterite, indicating that the SPEI film inhibits the crystallization of calcite. In Table 3, the percentages of vaterite and calcite in the $CaCO_3$ precipitates obtained are reported using the Kontoyannis equation [13] with its corresponding standard deviation. Notably, the presence of the PEI film increases the calcite phase, while SPEI inhibits it. Particularly, the SPEI film interacted strongly with Ca^{2+} ions, as evidenced by the results obtained in the APT curve, suggesting that the adsorption of calcium from the solution promotes the formation of vaterite. A $CaCO_3$ crystallization study varying the $[Ca^{2+}]/[CO_3^{2-}]$ ratio found that while a high ratio promotes the formation of calcite, a low ratio promotes vaterite, which could occur in this study due to calcium reduction [33]. However, the $CaCO_3$ crystallization process is very complex and further studies in the presence of these films are still needed.

On the other hand, in Fig. 7S, the XRD diffractograms of the PEI film before and after the $CaCO_3$ crystallization assays are shown. The broad diffraction peak confirms the amorphous

Preprint not peer reviewed

This preprint research paper has not been peer reviewed. Electronic copy available at: https://ssrn.com/abstract=4820270

nature of PEI and does not undergo any change during the crystallization assays. Contrary to the SPEI film in Fig. 8b, which, after the crystallization assays, shows crystallographic peaks at 2θ angles of 14.7°, 25.5°, and 29.6°. After comparison with the ICDD database, these were matched with #023-0128 corresponding to the hydrate of calcium sulfate $CaSO_4 \cdot 0.15H_2O$. The formation of this structure is possible due to the coordination of the sulfonic group with Ca^{2+} ions. The appearance of this phase was also observed in the sulfated ethylene-vinyl alcohol copolymer when treated with $Ca(OH)_2$ [34]. Cao and colleagues [35] suggest that SPEI could coordinate with divalent ions such as calcium ($-SO_3-M^{2+}-O_3S$), forming a packing arrangement that could generate a kind of ordering within the polymer as observed in the diffraction pattern.

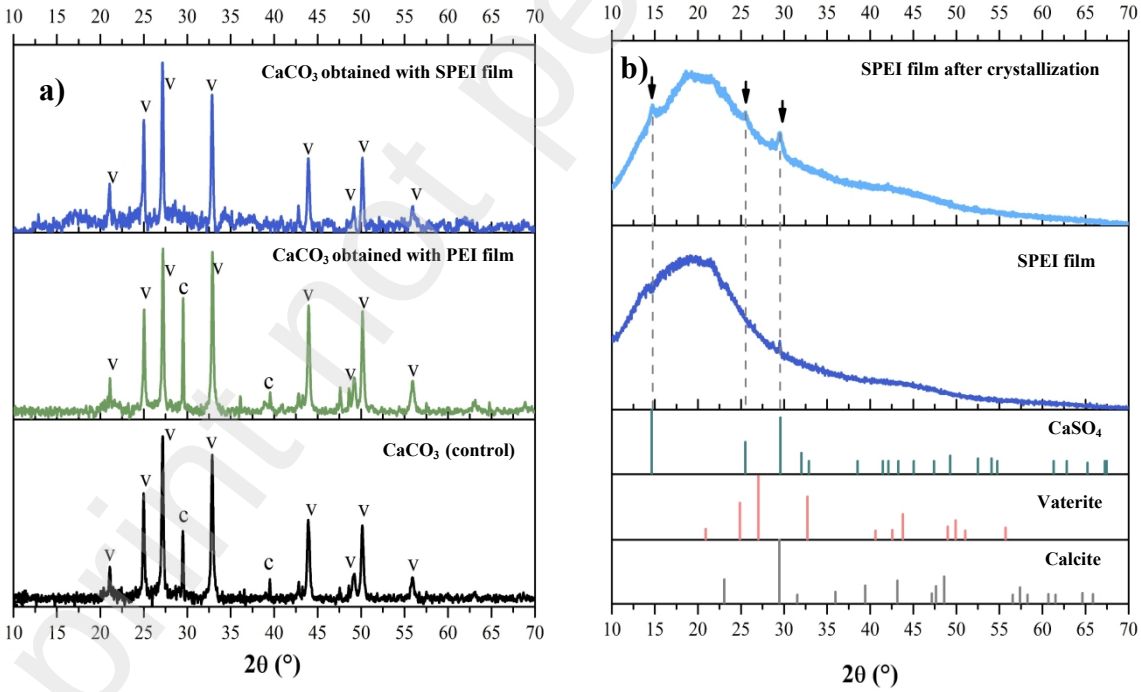

Fig. 8. XRD patterns of $CaCO_3$ obtained a) in absence (control) and presence of PEI and SPEI films, and b) SPEI film before and after the $CaCO_3$ crystallization assays.

Preprint not peer reviewed

This preprint research paper has not been peer reviewed. Electronic copy available at: https://ssrn.com/abstract=4820270

Table 3. Percentage of vaterite and calcite obtained after the $CaCO_3$ crystallization assays in the absence (control) and presence of PEI and SPEI films using the Kontoyannis equation [13].

Samples	Vaterite (%)	Calcite (%)
$CaCO_3$ (control)	91 ± 1	9 ± 1
$CaCO_3$ with PEI film	87.8 ± 0.4	12.2 ± 0.4
$CaCO_3$ with SPEI film	98 ± 2	2 ± 2

In Fig. 9 FESEM micrographs of the $CaCO_3$ obtained in the absence of films (Fig. 9a and 9b), in the presence of the PEI film (Fig. 9c and 9d), and SPEI film (Fig. 9e and 9f) are presented. In both the absence and presence of the films, similar $CaCO_3$ morphologies are observed. Spherical particles appear as complete spheres or disks and some rhombohedral particles, which correspond to the vaterite and calcite phases respectively, confirming the results from FTIR and XRD. Nanometric spheres of around 20 nm are also presented (see inset of Fig. 9b), which coincides with what has been reported for ACC particles [6] [36], confirming the FTIR results. In Fig. 9d, a calcite crystal surrounded by ACC is visible. Various studies suggest that calcite crystals may form by the agglomeration, dissolution, and recrystallization of ACC [37]. On the other hand, in Fig. 9f vaterite particles formed by polycrystalline disks are observed, a morphology previously reported [6] [38]. The above results indicate that the presence of the films does not have a distinctive effect on the morphology of the $CaCO_3$ precipitated from the APT crystallization assays.

Preprint not peer reviewed

This preprint research paper has not been peer reviewed. Electronic copy available at: https://ssrn.com/abstract=4820270

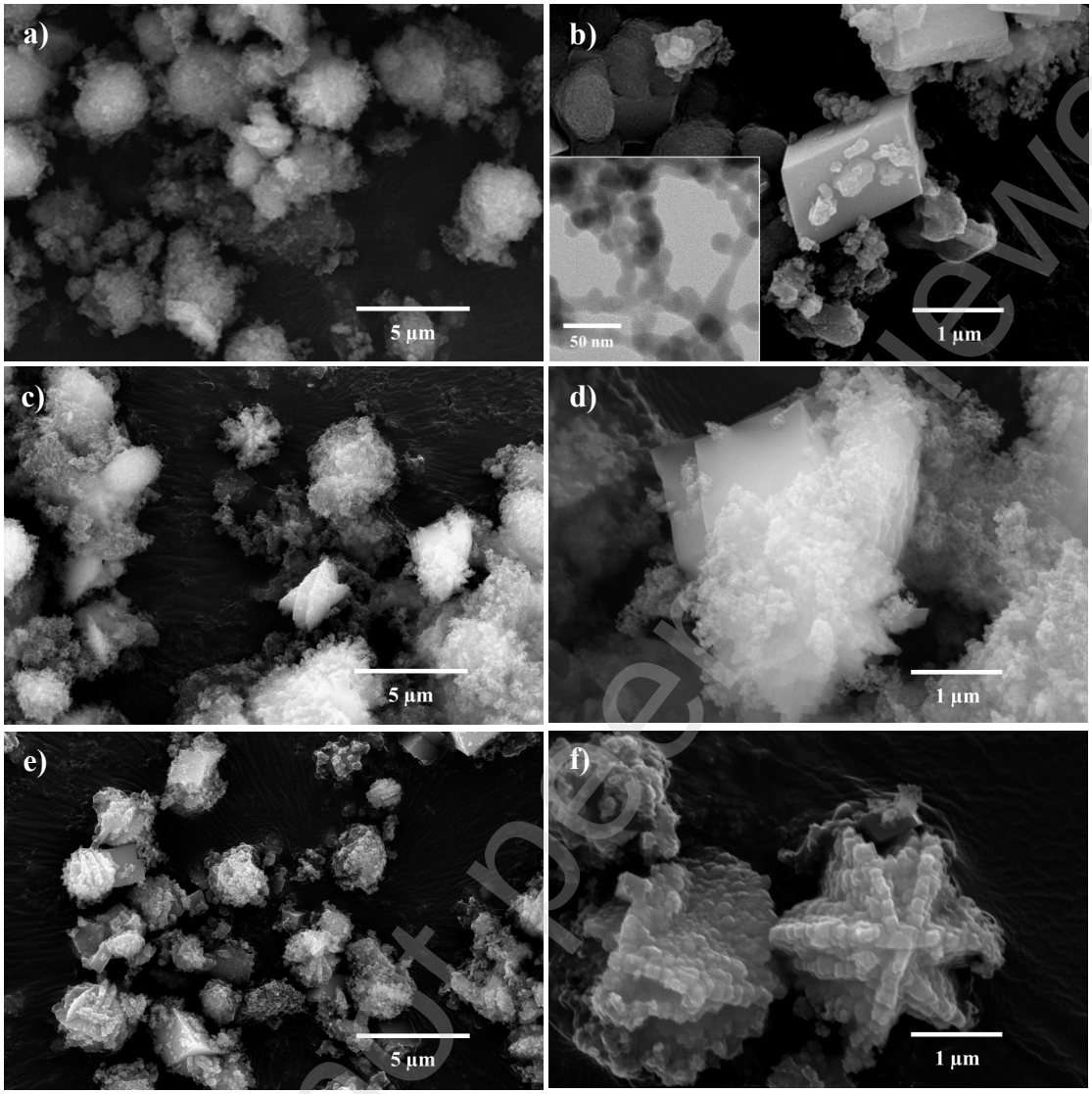

487

488 **Fig. 9.** Secondary electron FESEM micrographs of $CaCO_3$ obtained in absence of films (a
489 and b); in the presence of PEI film (c and d); and in the presences of SPEI film (e and f).
490 Inset b) transmission electron microscopy micrograph of ACC.

491

492 As we mentioned, the surfaces of the films produced by solvent casting were smooth and free
493 of any type of particles. After the $CaCO_3$ crystallization assays, different particles were found
494 on the surface of the films (Fig. 10). Fig. 10a presents the surface morphology of the PEI

Preprint not peer reviewed

This preprint research paper has not been peer reviewed. Electronic copy available at: https://ssrn.com/abstract=4820270

film after the crystallization assays, showing particles with two types of morphologies, spheres and rhombohedra, which coincide with the $CaCO_3$ precipitates associated with vaterite and calcite, respectively. No ACC particles were observed. The particle morphology shown in Fig. 10b has previously been found in vaterite crystals [39]. These researchers suggest a formation mechanism for these particles via ACC nanoparticles. Initially, ACC nanoparticles aggregate forming small hexagonal plates that later crystallize; then, the hexagonal plates join forming these superstructures. In Fig. 10c and 10d, a typical rhombohedral crystal of calcite is observed; its surface is smooth and flawless. Areas 1 and 2 indicated in the image were studied by energy-dispersive spectroscopy (EDS), and the results are shown in Table 4. The atomic ratio between Ca:C and Ca:O in both areas approximates 1:1 and 1:3, respectively, confirming the formation of $CaCO_3$. Generally, very few particles are found on the surface of the PEI film, which is related to the little interaction of this film with the crystallization medium, as evidenced by the unchanged APT curve of the PEI film compared to the control assay. The formation of crystals on the PEI film occurs because the film acts as an initial surface for nucleation considering that heterogeneous nucleation is energetically less demanding than homogeneous nucleation [33].

Preprint not peer reviewed

This preprint research paper has not been peer reviewed. Electronic copy available at: https://ssrn.com/abstract=4820270

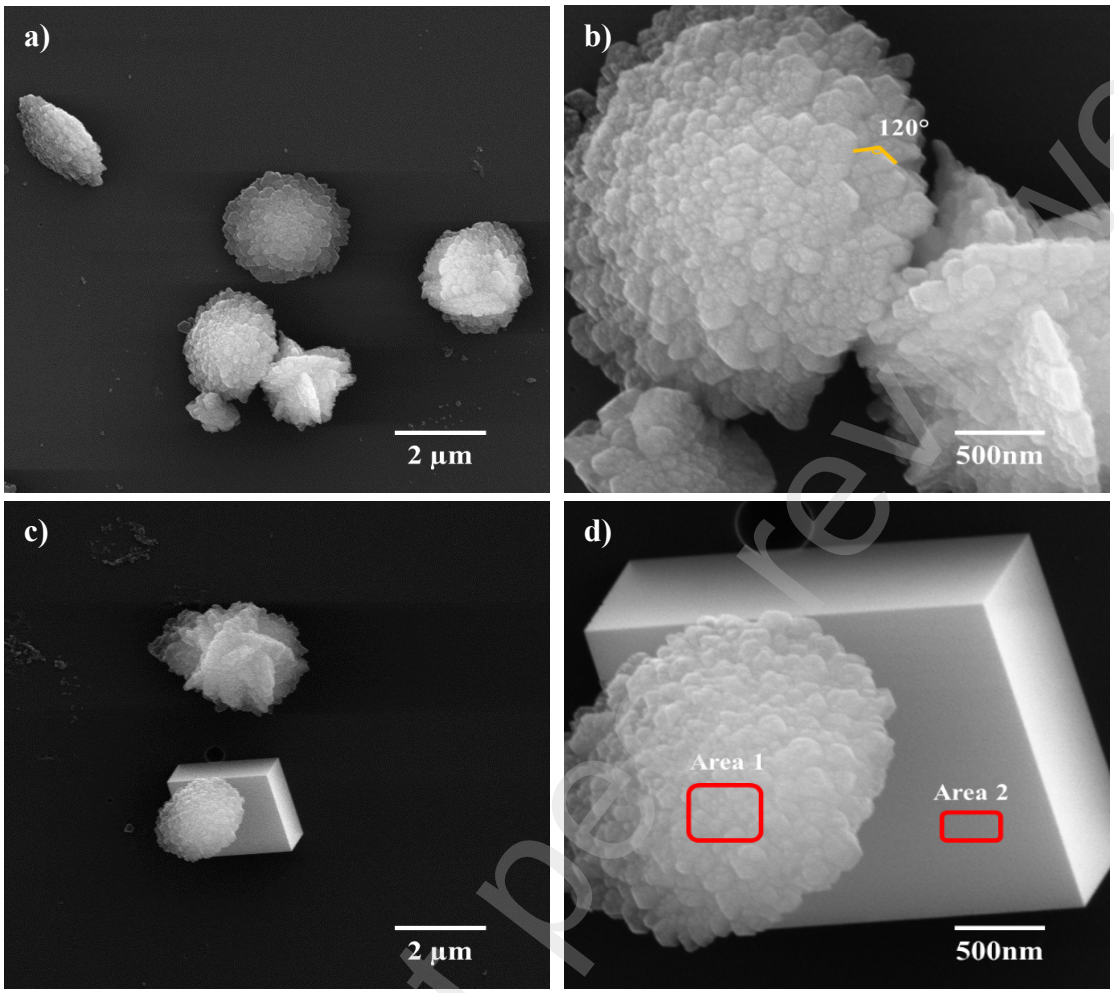

Fig. 10. Secondary electron FESEM micrographs of the PEI film after the $CaCO_3$ crystallization assays. (a and b) vaterite crystals; (c and d) vaterite and calcite crystals.

Fig. 11 shows the surface of the SPEI film and four different crystal morphologies after the crystallization assays. Fig. 11a and 11b show nanometric particles uniformly distributed across the film surface. The particles are approximately 58 ± 12 nm in size, without a defined shape, and seem to be formed by small spherical particles of about 20 nm, as indicated by the orange arrow. This coincides with the particles observed in the $CaCO_3$ precipitates associated with the ACC polymorph. The aggregation of similar particles was observed by Rodríguez-Navarro and colleagues [40] in studies of calcite crystallization through ACC

Preprint not peer reviewed

This preprint research paper has not been peer reviewed. Electronic copy available at: https://ssrn.com/abstract=4820270

nanoparticles; these aggregations were called ACC islands. In Fig. 11c and 11d, two types of morphologies can be observed, similar to those obtained on the PEI film (i.e., spherical and rhombohedral particles), possibly calcite and vaterite based on previous reports [6] [38] [39]. An interesting effect is observed around the spherical and rhombohedral particles— the absence of ACC, which is situated away from these. A similar observation was made by Lee and colleagues [41] in studies of $CaCO_3$ crystallization using self-assembled monolayers of mercaptophenol on gold. In this study, ACC precipitated on the study surface, and the researchers then observed that once calcite nucleated, a ring of ACC particles disappeared around the crystal. This demonstrates that the transformation process from ACC to calcite occurs through the dissolution of amorphous species and recrystallization, as has been observed by other authors and evidenced in the present study [42] [37]. Additionally, areas 3 and 4 indicated in the image were studied by EDS, and the results are reported in Table 4. In both areas (with and without ACC), Ca is detected, indicating that this element may be in ACC as well as in the film due to the formation of the complex with the sulfonic group observed in the FTIR results. Finally, a fourth morphology was observed on the films and is shown in Fig. 8Sa. Elongated surface relieves were found on the film, possibly corresponding to the $CaSO_4 \cdot 0.15H_2O$ found in the XRD studies. To confirm the formation of $CaSO_4 \cdot 0.15H_2O$ on the SPEI film, APT assays of Ca^{2+} adsorption were conducted by dosing $CaCl_2$ in water at pH 9, i.e., without carbonate and in the presence of the film. Subsequently, the film was studied by FTIR, XRD, and FESEM. In the FESEM micrograph in Fig. 8Sb, elongated and superficial reliefs were observed again on the film, confirming that this morphology does not correspond to $CaCO_3$, since the assay was conducted in the absence of carbonate, indicating that it corresponds to $CaSO_4 \cdot 0.15H_2O$.

Preprint not peer reviewed

This preprint research paper has not been peer reviewed. Electronic copy available at: https://ssrn.com/abstract=4820270

Table 4. Elemental composition by EDS of PEI film after the $CaCO_3$ crystallization assays.

Areas	Carbon		Oxygen		Sulfur		Calcium	
	% -wt.	% - at.	% -wt.	% - at.	% -wt.	% - at.	% -wt.	% - at.
1	11.15	19.78	41.18	54.87	0.00	0.00	47.67	25.35
2	11.07	18.90	46.14	59.19	0.00	0.00	42.79	21.91
3	72.74	80.32	20.66	17.13	4.34	1.8	2.26	0.76
4	72.85	80.90	19.31	16.10	4.86	2.01	2.99	1.00

On the other hand, the FTIR results shown in Fig. 9S confirm the formation of complexes between the sulfonic group and Ca^{2+} ions due to changes in intensity and band shifts as explained. Additionally, the three morphologies of $CaCO_3$ particles obtained in the precipitates were not observed. Finally, in the XRD results shown in Fig. 10S, diffraction peaks corresponding to $CaSO_4 \cdot 0.15H_2O$ crystals in the film confirm their presence.

Preprint not peer reviewed

This preprint research paper has not been peer reviewed. Electronic copy available at: https://ssrn.com/abstract=4820270

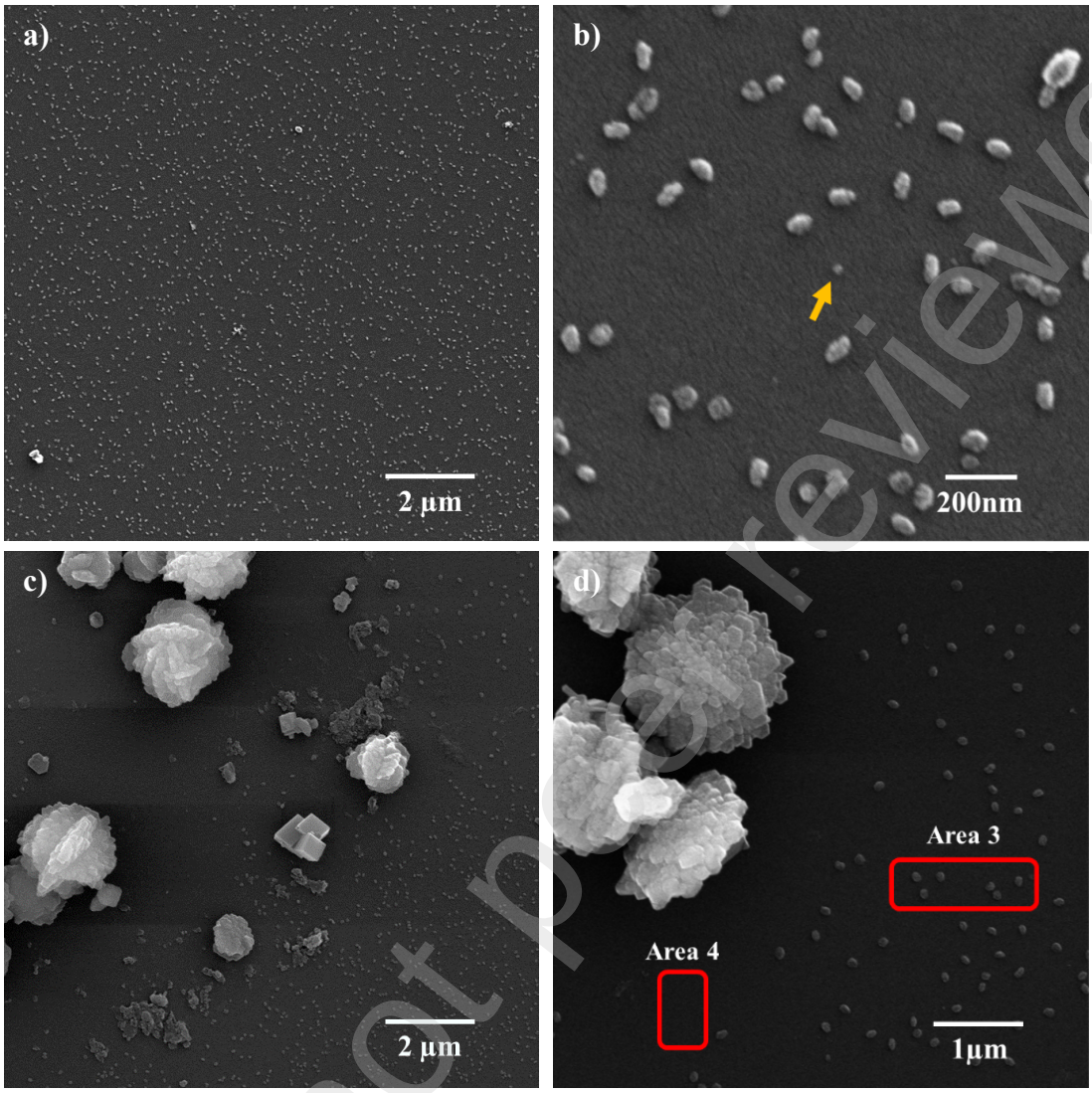

Fig. 11. Secondary electron FESEM micrographs of the SPEI film after the $CaCO_3$ crystallization assays. (a and b) ACC particles; (c and d) vaterite and calcite crystals and ACC particles.

3.5 Proposed mechanisms of nucleation and crystallization of $CaCO_3$ on PEI and SPEI films

Considering the APT curves obtained from the $CaCO_3$ crystallization assays in the absence (control) and presence of PEI and SPEI films and characterization techniques, a tentative mechanism for nucleation inhibition, PNC capture, and ACC formation on the SPEI film

Preprint not peer reviewed

This preprint research paper has not been peer reviewed. Electronic copy available at: https://ssrn.com/abstract=4820270

(Fig. 12) is proposed. Fig. 12 shows numerous results. (a) During the immersion of the SPEI film in the CO_3^{2-} buffer solution, Ca^{2+} is slowly added and the presence of negatively charged sulfonic groups interact and attract the Ca^{2+} cations. (b) Given that according to Z potential results it is possible that the film absorbs water, the formation of complexes between the sulfonic group and calcium may occur on the surface of the film as well as inside it. The formation of these complexes results in the reduction of free calcium in the solution, which induces a decrease in the initial slope of the APT curve. This interaction with calcium allows the capture of PNC formed in the solution. (c) The PNC aggregate and grow on the surface of the film, reducing the free calcium in the solution, as reflected in a second decrease in the slope of the APT curve. The reduction of free calcium causes a longer nucleation time to reach maximum saturation. (d) The aggregation of clusters forms larger particles that nucleate into ACC. (e) Finally, the ACC particles nucleated on the surface of the film, and those suspended in the solution form larger particles like ACC islands. This demonstrates the value of the APT method applied in $CaCO_3$ crystallization studies in the presence of insoluble polymer surfaces.

Preprint not peer reviewed

This preprint research paper has not been peer reviewed. Electronic copy available at: https://ssrn.com/abstract=4820270

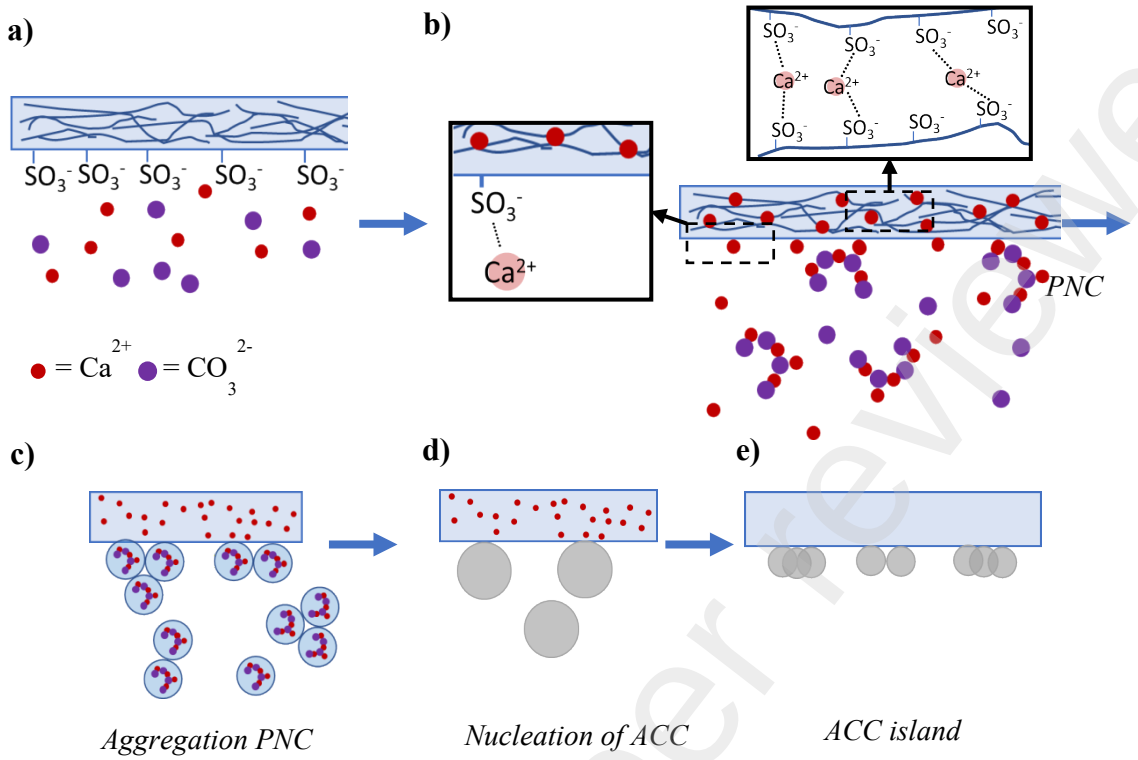

583

584 **Fig. 12.** Proposed mechanism of Ca^{2+} adsorption, PNC capture, and ACC formation on the

585 SPEI film.

586

587 Additionally, regarding the formation of crystals on the surface of PEI and SPEI films, Fig.

588 13 shows different mechanisms. (a) According to classical nucleation theory, crystals could

589 form by the union of ions and crystallization. (b) ACC particles on the films (in the case of

590 SPEI film) and in the solution could aggregate and transform into calcite and vaterite crystals

591 through dissolution-recrystallization on the films. (c) Regarding vaterite, hexagonal plates

592 could form on the films or in the solution and join, forming these superstructures on the

593 surface of the polymer. (d) Specifically for the SPEI film, it is possible that the ACC islands

594 formed on its surface contribute to the formation and growth of vaterite and calcite crystals

595 through dissolution-recrystallization.

596

Preprint not peer reviewed

This preprint research paper has not been peer reviewed. Electronic copy available at: https://ssrn.com/abstract=4820270

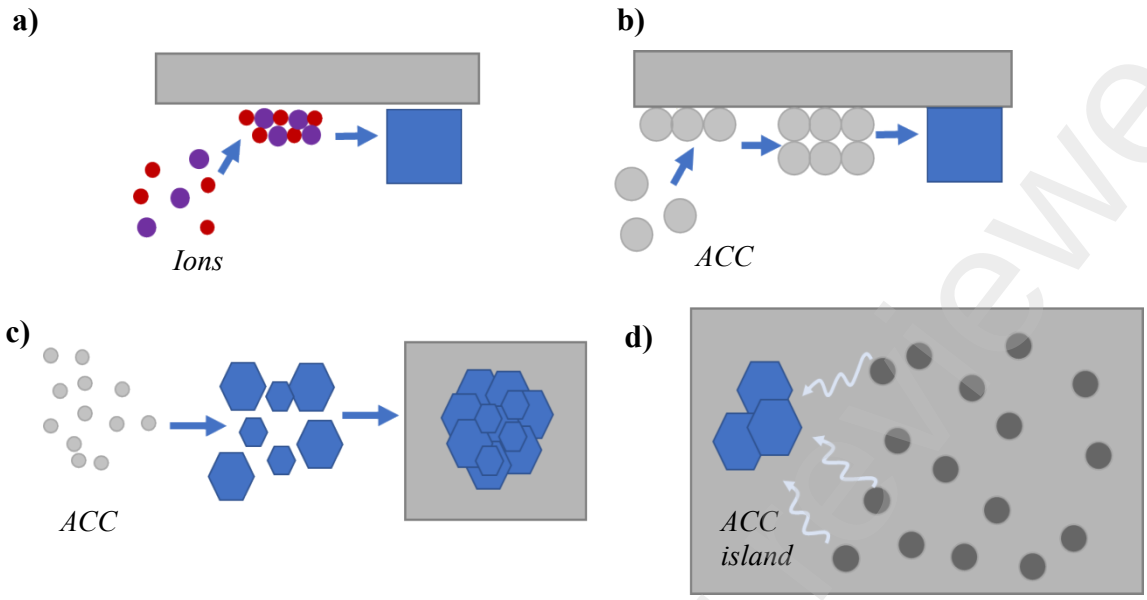

Fig. 13. Proposed mechanism of $CaCO_3$ crystal formation on PEI and SPEI films.

4. Conclusions

The APT method proved to be a valuable tool for studying the phenomena involved in the $CaCO_3$ crystallization process in the presence of polymeric surfaces of PEI and SPEI obtained by solvent casting. A comprehensive surface characterization was performed on the films using FESEM, XPS, Z potential, and contact angle. The films exhibited a smooth, homogeneous surface without cracks. Confirmed by XPS was the presence of the sulfonic group on the surface of the SPEI film, while Z potential and contact angle measurements indicated hydrophilic properties compared to the PEI film. APT assays on PEI and SPEI films indicate that the PEI film did not interact with Ca^{2+} as the APT curve showed no change compared to the control assay. On the other hand, the SPEI film had an inhibitory effect on the nucleation of $CaCO_3$ by decreasing the free calcium in the solution, affecting the time to reach maximum saturation through the formation of complexes with calcium and capture of PNC, as evidenced by changes in the slope of the APT curves and confirmed by subsequent

Preprint not peer reviewed

This preprint research paper has not been peer reviewed. Electronic copy available at: https://ssrn.com/abstract=4820270

studies of the films with FTIR, FESEM, and XRD. Additionally, the $CaCO_3$ precipitate after the APT assays was studied, finding that the SPEI film inhibits the formation of calcite in the solution. In summary, the APT method could be projected for studies on surfaces for water softening, desalination membranes, and reverse osmosis membranes, among others, providing valuable information about the phenomena occurring on the surface of the material.

CRediT authorship contribution statement

Estefanía Correa-Muñoz: Conceptualization, Methodology, Validation, Investigation Resources, Writing - Original Draft, Funding acquisition. **Nicole Butto-Miranda:** Methodology. **Nicole Parra-Muñoz:** Methodology, Resources. **Adriana Blanco-Leal:** Methodology. **Alejandra Santa-Arango:** Methodology. **Felipe Díaz-Soler:** Methodology. **Mehrdad Yazdani-Pedram:** Resources, Writing - Original Draft. **Carlos Ostos-Ortiz:** Methodology, Resources. **Gustavo Cabrera-Barjas:** Resources, Data curation, Review&Editing. **Franscisco Gracia:** Resources. **Andrónico Neira-Carrillo:** Conceptualization, Methodology, Investigation, Resources, Writing - Original Draft, Supervision, Writing - Review & Editing, Funding acquisition.

Declaration of Competing Interest

The authors declare that they have no known competing financial interests or personal relationships that could have appeared to influence the work reported in this paper.

Data availability

Data will be made available on request.

Preprint not peer reviewed

This preprint research paper has not been peer reviewed. Electronic copy available at: https://ssrn.com/abstract=4820270

Acknowledgments

This work was funded by ANID through Regular Fondecyt Project Nº 1211345. The authors are grateful for financial support to Minciencias-Colombia for the Doctorado en el exterior-860 2019 scholarship; ANID -Chile for the Doctorado Nacional 2020 - Folio: 21182122; and the Fondecyt Postdoctorate Project Nº 3200610.

References

[1] A. Hulanicki, M. Maj-Żurawska, S. Glab, TITRIMETRY | Potentiometry, in: Ref. Modul. Chem. Mol. Sci. Chem. Eng., Elsevier, 2013. https://doi.org/10.1016/B978-0-12-409547-2.00546-1.

[2] D. Gebauer, A. Völkel, H. Cölfen, Stable prenucleation calcium carbonate clusters, Science (80-.). 322 (2008) 1819–1822. https://doi.org/10.1126/science.1164271.

[3] D. Gebauer, H. Cölfen, A. Verch, M. Antonietti, The multiple roles of additives in $CaCO_3$ crystallization: A quantitative case study, Adv. Mater. 21 (2009) 435–439. https://doi.org/10.1002/adma.200801614.

[4] A. Picker, M. Kellermeier, J. Seto, D. Gebauer, H. Cölfen, The multiple effects of amino acids on the early stages of calcium carbonate crystallization, in: Zeitschrift Fur Krist., 2012: pp. 744–757. https://doi.org/10.1524/zkri.2012.1569.

[5] A. Verch, D. Gebauer, M. Antonietti, H. Cölfen, How to control the scaling of $CaCO_3$: A “fingerprinting technique” to classify additives, Phys. Chem. Chem. Phys. 13 (2011) 16811–16820. https://doi.org/10.1039/c1cp21328h.

[6] D. Gebauer, A. Verch, H.G. Börner, H. Cölfen, Influence of selected artificial peptides on calcium carbonate precipitation - A quantitative studyp, Cryst. Growth Des. 9 (2009) 2398–2403. https://doi.org/10.1021/cg801292p.

Preprint not peer reviewed

This preprint research paper has not been peer reviewed. Electronic copy available at: https://ssrn.com/abstract=4820270

[7] M. Sánchez, P. Vásquez-Quitral, N. Butto, F. Díaz-Soler, M. Yazdani-Pedram, J.F. Silva, A. Neira-Carrillo, Effect of alginate from chilean lessonia nigrescens and MWCNTs on $CaCO_3$ crystallization by classical and non-classical methods, Crystals. 8 (2018). https://doi.org/10.3390/cryst8020069.

[8] Y. Hu, Y. Xu, M. Xie, M. Huang, G. Chen, Characterization of scalants and strategies for scaling mitigation in membrane distillation of alkaline concentrated circulating cooling water, Desalination. 527 (2022) 115534. https://doi.org/10.1016/j.desal.2021.115534.

[9] N.R. Sarker, P. Cherukupally, I. Gourevich, J. Wilbur, S.D. Jons, A.M. Bilton, Multi-scale visualization of incipient CaCO3 scaling on the polyamide layer of reverse osmosis membranes, Desalination. 539 (2022) 115956. https://doi.org/10.1016/j.desal.2022.115956.

[10] W. Mao, Y. Gu, W. Kang, H. Yu, Facilitated OH^- diffusion via bubble motion and water flow in a novel electrochemical reactor for enhancing homogeneous nucleation of $CaCO_3$, Water Res. 242 (2023) 120195. https://doi.org/10.1016/j.watres.2023.120195.

[11] K. Fanourakis, Y. Hu, A. Ansari, J. Pe, D.F. Rodrigues, Microbially-induced mineral scaling in desalination conditions : Mechanisms and effects of commercial antiscalants, 179 (2020). https://doi.org/10.1016/j.watres.2020.115863.

[12] M. Rajagopalan, J.H. Jeon, I.K. Oh, Electric-stimuli-responsive bending actuator based on sulfonated polyetherimide, Sensors Actuators, B Chem. 151 (2010) 198–204. https://doi.org/10.1016/j.snb.2010.09.021.

[13] C.G. Kontoyannis, N. V. Vagenas, Calcium carbonate phase analysis using XRD and FT-Raman spectroscopy, Analyst. 125 (2000) 251–255.

Preprint not peer reviewed

This preprint research paper has not been peer reviewed. Electronic copy available at: https://ssrn.com/abstract=4820270

https://doi.org/10.1039/a908609i.

[14] S. Guhathakurta, K. Min, Influence of crystal morphology of 1H-1,2,4-triazole on anhydrous state proton conductivity of sulfonated bisphenol A polyetherimide based polyelectrolytes, Polymer (Guildf). 50 (2009) 1034–1045. https://doi.org/10.1016/j.polymer.2008.12.035.

[15] V. Deimede, G.A. Voyiatzis, J.K. Kallitsis, L. Qingfeng, N.J. Bjerrum, Miscibility behavior of polybenzimidazole/sulfonated polysulfone blends for use in fuel cell applications, Macromolecules. 33 (2000) 7609–7617. https://doi.org/10.1021/ma000165s.

[16] M. Kaba, N. Raklaoui, M.-F. Guimon, A. Mas, Improvement of the water selectivity of ULTEM poly(ether imide) pervaporation films by an allylamine-plasma-polymerized layer, J. Appl. Polym. Sci. 97 (2005) 2088–2096. https://doi.org/10.1002/app.21684.

[17] M.C. Burrell, J.J. Chera, Polyetherimide (Ultem®) spin cast films by XPS, Surf. Sci. Spectra. 6 (1999) 18–22. https://doi.org/10.1116/1.1247898.

[18] G. Pellegrino, S.C. Carroccio, F. Ruffino, G.G. Condorelli, G. Nicotra, V. Privitera, G. Impellizzeri, Polymeric platform for the growth of chemically anchored ZnO nanostructures by ALD, RSC Adv. 8 (2018) 521–530. https://doi.org/10.1039/c7ra11168a.

[19] M. Feng, Y. Feng, Z. Yang, T. Zhang, Q. Chi, Q. Lei, Effect of humidity on the microstructure and energy storage properties of polyetherimide, Appl. Phys. Lett. 119 (2021) 1–6. https://doi.org/10.1063/5.0066003.

[20] N. Bolong, A.F. Ismail, M.R. Salim, D. Rana, T. Matsuura, Surface characterization by X–Ray photoelectron spectroscopy of polyethersulfone hollow fiber membranes

Preprint not peer reviewed

This preprint research paper has not been peer reviewed. Electronic copy available at: https://ssrn.com/abstract=4820270

709 modified with surface modifying macromolecules, J. Appl. Membr. Sci. Technol. 11
710 (2017) 25–33. https://doi.org/10.11113/amst.v11i1.77.
711 [21] X.L. Wei, M. Fahlman, A.J. Epstein, XPS study of highly sulfonated polyaniline,
712 Macromolecules. 32 (1999) 3114–3117. https://doi.org/10.1021/ma981386p.
713 [22] W. Wang, H. Wang, X. Jin, H. Wang, T. Lin, Z. Zhu, Effects of hydrogen bonding
714 on starch granule dissolution, spinnability of starch solution, and properties of
715 electrospun starch fibers, Polymer (Guildf). 153 (2018) 643–652.
716 https://doi.org/10.1016/j.polymer.2018.08.067.
717 [23] M.G. McKee, C.L. Elkins, T.E. Long, Influence of self-complementary hydrogen
718 bonding on solution rheology/electrospinning relationships, Polymer (Guildf). 45
719 (2004) 8705–8715. https://doi.org/10.1016/j.polymer.2004.10.049.
720 [24] A.J. Pertsin, M.M. Gorelova, V.Y. Levin, L.I. Makarova, An XPS study of the
721 surface–bulk compositional differences in siloxane-containing block copolymers and
722 polymer blends, J. Appl. Polym. Sci. 45 (1992) 1195–1202.
723 https://doi.org/10.1002/app.1992.070450708.
724 [25] C. Chan, L.-T. Weng, Surface characterization of polymer blends by XPS and ToF-
725 SIMS, Materials (Basel). 9 (2016) 655. https://doi.org/10.3390/ma9080655.
726 [26] S. Saedi, S.S. Madaeni, A.A. Shamsabadi, Fabrication of asymmetric
727 polyethersulfone membranes for separation of carbon dioxide from methane using
728 polyetherimide as polymeric additive, Chem. Eng. Res. Des. 92 (2014) 2431–2438.
729 https://doi.org/10.1016/j.cherd.2014.02.010.
730 [27] S. Gassara, W. Chinpa, D. Quemener, R. Ben Amar, A. Deratani, Pore size tailoring
731 of poly(ether imide) membrane from UF to NF range by chemical post-treatment
732 using aminated oligomers, J. Memb. Sci. 436 (2013) 36–46.

Preprint not peer reviewed

This preprint research paper has not been peer reviewed. Electronic copy available at: https://ssrn.com/abstract=4820270

https://doi.org/10.1016/j.memsci.2013.02.005.

[28] T. Luxbacher, The zeta potential for solid surface analysis. A practical guide to streaming potential measurement, 1st editio, Anton Paar GmbH, Austria, 2014.

[29] D. Gebauer, P.N. Gunawidjaja, J.Y.P. Ko, Z. Bacsik, B. Aziz, L. Liu, Y. Hu, L. Bergström, C.W. Tai, T.K. Sham, M. Edén, N. Hedin, Proto-calcite and proto-vaterite in amorphous calcium carbonates, Angew. Chemie - Int. Ed. 49 (2010) 8889–8891. https://doi.org/10.1002/anie.201003220.

[30] P.J.M. Smeets, K.R. Cho, R.G.E. Kempen, N.A.J.M. Sommerdijk, J.J. De Yoreo, Calcium carbonate nucleation driven by ion binding in a biomimetic matrix revealed by in situ electron microscopy, Nat. Mater. 14 (2015) 394–399. https://doi.org/10.1038/nmat4193.

[31] Y. Zhou, R. Bosman, P.M. Lugt, On the shear stability of dry and water-contaminated calcium sulfonate complex lubricating greases, Tribol. Trans. 62 (2019) 626–634. https://doi.org/10.1080/10402004.2019.1588445.

[32] D. Yuan, S. Lei, L. Gao, Y. Liu, G. Liu, C. Wang, Mechanism study on the formation of complex between Ca(II) and indigo carmine for potential food use as a colorant lake, Food Chem. 322 (2020) 126709. https://doi.org/10.1016/j.foodchem.2020.126709.

[33] F.C. Meldrum, H. Cölfen, Controlling mineral morphologies and structures in biological and synthetic systems, Chem. Rev. 108 (2008) 4332–4432. https://doi.org/10.1021/cr8002856.

[34] I.B. Leonor, H.M. Kim, F. Balas, M. Kawashita, R.L. Reis, T. Kokubo, T. Nakamura, Functionalization of different polymers with sulfonic groups as a way to coat them with a biomimetic apatite layer, J. Mater. Sci. Mater. Med. 18 (2007)

Preprint not peer reviewed

This preprint research paper has not been peer reviewed. Electronic copy available at: https://ssrn.com/abstract=4820270

1923–1930. https://doi.org/10.1007/s10856-007-3106-6.

[35] K. Cao, J.M. Serrano, T. Liu, B.J. Stovall, Z. Xu, C.B. Arrington, T.E. Long, R.R. Odle, G. Liu, Impact of metal cations on the thermal, mechanical, and rheological properties of telechelic sulfonated polyetherimides, Polym. Chem. 11 (2020) 393–400. https://doi.org/10.1039/c9py00899c.

[36] T. Wang, M. Antonietti, H. Cölfen, Calcite mesocrystals: "Morphing" crystals by a polyelectrolyte, Chem. - A Eur. J. 12 (2006) 5722–5730. https://doi.org/10.1002/chem.200501019.

[37] A. Gal, K. Kahil, N. Vidavsky, R.T. Devol, P.U.P.A. Gilbert, P. Fratzl, S. Weiner, L. Addadi, Particle accretion mechanism underlies biological crystal growth from an amorphous precursor phase, Adv. Funct. Mater. 24 (2014) 5420–5426. https://doi.org/10.1002/adfm.201400676.

[38] A. Burgos-Cara, C. Putnis, C. Rodriguez-Navarro, E. Ruiz-Agudo, Hydration effects on the stability of calcium carbonate pre-nucleation species, Minerals. 7 (2017) 126. https://doi.org/10.3390/min7070126.

[39] A.W. Xu, M. Antonietti, H. Cölfen, Y.P. Fang, Uniform hexagonal plates of vaterite $CaCO_3$ mesocrystals formed by biomimetic mineralization, Adv. Funct. Mater. 16 (2006) 903–908. https://doi.org/10.1002/adfm.200500716.

[40] C. Rodriguez-Navarro, A. Burgos Cara, K. Elert, C. V. Putnis, E. Ruiz-Agudo, Direct nanoscale imaging reveals the growth of calcite crystals via amorphous nanoparticles, Cryst. Growth Des. 16 (2016) 1850–1860. https://doi.org/10.1021/acs.cgd.5b01180.

[41] J.R.I. Lee, T.Y.J. Han, T.M. Willey, D. Wang, R.W. Meulenberg, J. Nilsson, P.M. Dove, L.J. Terminello, T. Van Buuren, J.J. De Yoreo, Structural development of

Preprint not peer reviewed

This preprint research paper has not been peer reviewed. Electronic copy available at: https://ssrn.com/abstract=4820270

mercaptophenol self-assembled monolayers and the overlying mineral phase during templated $CaCO_3$ crystallization from a transient amorphous film, J. Am. Chem. Soc. 129 (2007) 10370–10381. https://doi.org/10.1021/ja071535w.

[42] D. Gebauer, How can additives control the early stages of mineralisation?, Minerals. 8 (2018). https://doi.org/10.3390/min8050179.

Preprint not peer reviewed

This preprint research paper has not been peer reviewed. Electronic copy available at: https://ssrn.com/abstract=4820270